Anthropogenic emissions of methane in the United States

Scot M. Miller[a,1], Steven C. Wofsy[a], Anna M. Michalak[b], Eric A. Kort[c], Arlyn E. Andrews[d], Sebastien C. Biraud[e], Edward J. Dlugokencky[d], Janusz Eluszkiewicz[f], Marc L. Fischer[g], Greet Janssens-Maenhout[h], Ben R. Miller[i], John B. Miller[i], Stephen A. Montzka[d], Thomas Nehrkorn[f], and Colm Sweeney[i]

[a]Department of Earth and Planetary Sciences, Harvard University, Cambridge, MA 02138; [b]Department of Global Ecology, Carnegie Institution for Science, Stanford, CA 94305; [c]Department of Atmospheric, Ocean, and Space Sciences, University of Michigan, Ann Arbor, MI 48109; [d]Global Monitoring Division, Earth System Research Laboratory, National Oceanic and Atmospheric Administration, Boulder, CO 80305; [e]Earth Sciences Division, and [g]Environmental Energy Technologies Division, Lawrence Berkeley National Laboratory, Berkeley, CA 94720; [f]Atmospheric and Environmental Research, Lexington, MA 02421; [h]Institute for Environment and Sustainability, European Commission Joint Research Centre, 21027 Ispra, Italy; and [i]Cooperative Institute for Research in Environmental Sciences, University of Colorado Boulder, Boulder, CO 80309

This study quantitatively estimates the spatial distribution of anthropogenic methane sources in the United States by combining comprehensive atmospheric methane observations, extensive spatial datasets, and a high-resolution atmospheric transport model. Results show that current inventories from the US Environmental Protection Agency (EPA) and the Emissions Database for Global Atmospheric Research underestimate methane emissions nationally by a factor of ~1.5 and ~1.7, respectively. Our study indicates that emissions due to ruminants and manure are up to twice the magnitude of existing inventories. In addition, the discrepancy in methane source estimates is particularly pronounced in the south-central United States, where we find total emissions are ~2.7 times greater than in most inventories and account for 24 ± 3% of national emissions. The spatial patterns of our emission fluxes and observed methane–propane correlations indicate that fossil fuel extraction and refining are major contributors (45 ± 13%) in the south-central United States. This result suggests that regional methane emissions due to fossil fuel extraction and processing could be 4.9 ± 2.6 times larger than in EDGAR, the most comprehensive global methane inventory. These results cast doubt on the US EPA's recent decision to downscale its estimate of national natural gas emissions by 25–30%. Overall, we conclude that methane emissions associated with both the animal husbandry and fossil fuel industries have larger greenhouse gas impacts than indicated by existing inventories.

climate change policy | geostatistical inverse modeling

Methane (CH_4) is the second most important anthropogenic greenhouse gas, with approximately one third the total radiative forcing of carbon dioxide (1). CH_4 also enhances the formation of surface ozone in populated areas, and thus higher global concentrations of CH_4 may significantly increase ground-level ozone in the Northern Hemisphere (2). Furthermore, methane affects the ability of the atmosphere to oxidize other pollutants and plays a role in water formation within the stratosphere (3).

Atmospheric concentrations of CH_4 [~1,800 parts per billion (ppb)] are currently much higher than preindustrial levels (~680–715 ppb) (1, 4). The global atmospheric burden started to rise rapidly in the 18th century and paused in the 1990s. Methane levels began to increase again more recently, potentially from a combination of increased anthropogenic and/or tropical wetland emissions (5–7). Debate continues, however, over the causes behind these recent trends (7, 8).

Anthropogenic emissions account for 50–65% of the global CH_4 budget of ~395–427 teragrams of carbon per year ($TgC \cdot y^{-1}$) (526–569 Tg CH_4) (7, 9). The US Environmental Protection Agency (EPA) estimates the principal anthropogenic sources in the United States to be (in order of importance) (*i*) livestock (enteric fermentation and manure management), (*ii*) natural gas

production and distribution, (*iii*) landfills, and (*iv*) coal mining (10). EPA assesses human-associated emissions in the United States in 2008 at 22.1 TgC, roughly 5% of global emissions (10).

The amount of anthropogenic CH_4 emissions in the US and attributions by sector and region are controversial (Fig. 1). Bottom-up inventories from US EPA and the Emissions Database for Global Atmospheric Research (EDGAR) give totals ranging from 19.6 to 30 $TgC \cdot y^{-1}$ (10, 11). The most recent EPA and EDGAR inventories report lower US anthropogenic emissions compared with previous versions (decreased by 10% and 35%, respectively) (10, 12); this change primarily reflects lower, revised emissions estimates from natural gas and coal production Fig. S1. However, recent analysis of CH_4 data from aircraft estimates a higher budget of 32.4 ± 4.5 $TgC \cdot y^{-1}$ for 2004 (13). Furthermore, atmospheric observations indicate higher emissions in natural gas production areas (14–16); a steady 20-y increase in the number of US wells and newly-adopted horizontal drilling techniques may have further increased emissions in these regions (17, 18).

These disparities among bottom-up and top-down studies suggest much greater uncertainty in emissions than typically reported. For example, EPA cites an uncertainty of only ±13% for the for United States (10). Independent assessments of bottom-up inventories give error ranges of 50–100% (19, 20), and

Significance

Successful regulation of greenhouse gas emissions requires knowledge of current methane emission sources. Existing state regulations in California and Massachusetts require ~15% greenhouse gas emissions reductions from current levels by 2020. However, government estimates for total US methane emissions may be biased by 50%, and estimates of individual source sectors are even more uncertain. This study uses atmospheric methane observations to reduce this level of uncertainty. We find greenhouse gas emissions from agriculture and fossil fuel extraction and processing (i.e., oil and/or natural gas) are likely a factor of two or greater than cited in existing studies. Effective national and state greenhouse gas reduction strategies may be difficult to develop without appropriate estimates of methane emissions from these source sectors.
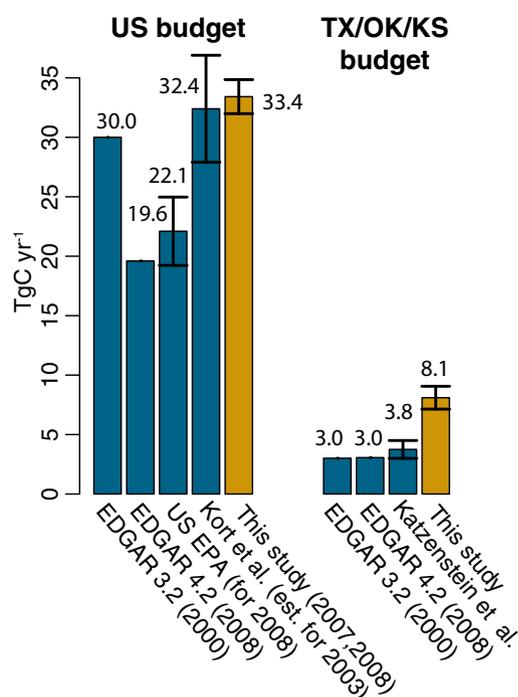
Fig. 1. US anthropogenic methane budgets from this study, from previous top-down estimates, and from existing emissions inventories. The south-central United States includes Texas, Oklahoma, and Kansas. US EPA estimates only national, not regional, emissions budgets. Furthermore, national budget estimates from EDGAR, EPA, and Kort et al. (13) include Alaska and Hawaii whereas this study does not.

values from Kort et al. are 47 ± 20% higher than EPA (13). Assessments of CH_4 sources to inform policy (e.g., regulating emissions or managing energy resources) require more accurate, verified estimates for the United States.

This study estimates anthropogenic CH_4 emissions over the United States for 2007 and 2008 using comprehensive CH_4 observations at the surface, on telecommunications towers, and from aircraft, combined with an atmospheric transport model and a geostatistical inverse modeling (GIM) framework. We use auxiliary spatial data (e.g., on population density and economic activity) and leverage concurrent measurements of alkanes to help attribute emissions to specific economic sectors. The work provides spatially resolved CH_4 emissions estimates and associated uncertainties, as well as information by source sector, both previously unavailable.

Model and Observation Framework

We use the Stochastic Time-Inverted Lagrangian Transport model (STILT) to calculate the transport of CH_4 from emission points at the ground to measurement locations in the atmosphere (21). STILT follows an ensemble of particles backward in time, starting from each observation site, using wind fields and turbulence modeled by the Weather Research and Forecasting (WRF) model (22). STILT derives an influence function ("footprint," units: ppb CH_4 per unit emission flux) linking upwind emissions to each measurement. Inputs of CH_4 from surface sources along the ensemble of back-trajectories are averaged to compute the CH_4 concentration for comparison with each observation.

We use observations for 2007 and 2008 from diverse locations and measurement platforms. The principal observations derive from daily flask samples on tall towers (4,984 total observations) and vertical profiles from aircraft (7,710 observations). Tower-based observations are collected as part of the National Oceanic and Atmospheric (NOAA)/Department of Energy (DOE)

cooperative air sampling network, and aircraft-based data are obtained from regular NOAA flights (23), regular DOE flights (24), and from the Stratosphere-Troposphere Analyses of Regional Transport 2008 (START08) aircraft campaign (25); all data are publicly available from NOAA and DOE. These observations are displayed in Fig. 2 and discussed further in the *SI Text* (e.g., Fig. S2). We use a GIM framework (26, 27) to analyze the footprints for each of the 12,694 observations, and these footprints vary by site and with wind conditions. In aggregate, the footprints provide spatially resolved coverage of most of the continental United States, except the southeast coastal region (Fig. S3).

The GIM framework, using footprints and concentration measurements, optimizes CH_4 sources separately for each month of 2007 and 2008 on a 1° × 1° latitude–longitude grid for the United States. The contributions of fluxes from natural wetlands are modeled first and subtracted from the observed CH_4 (2.0 $TgC·y^{-1}$ for the continental United States); these fluxes are much smaller than anthropogenic sources in the United States and thus would be difficult to independently constrain from atmospheric data (*SI Text*).

The GIM framework represents the flux distribution for each month using a deterministic spatial model plus a stochastic spatially correlated residual, both estimated from the atmospheric observations. The deterministic component is given by a weighted linear combination of spatial activity data from the EDGAR 4.2 inventory; these datasets include any economic or demographic data that may predict the distribution of CH_4 emissions (e.g., gas production, human and ruminant population densities, etc.). Both the selection of the activity datasets to be retained in the model and the associated weights (emission factors) are optimized to best match observed CH_4 concentrations. Initially, seven activity datasets are included from EDGAR 4.2, (*i*) population, (*ii*) electricity production from power plants, (*iii*) ruminant population count, (*iv*) oil and conventional gas production, (*v*) oil refinery production, (*vi*) rice production, and (*vii*) coal production.

We select the minimum number of datasets with the greatest predictive ability using the Bayesian Information Criterion (BIC) (*SI Text*) (28). BIC numerically scores all combinations of available datasets based on how well they improve goodness of fit and applies a penalty that increases with the number of datasets retained.

The stochastic component represents sources that do not fit the spatial patterns of the activity data (Fig. S4). GIM uses
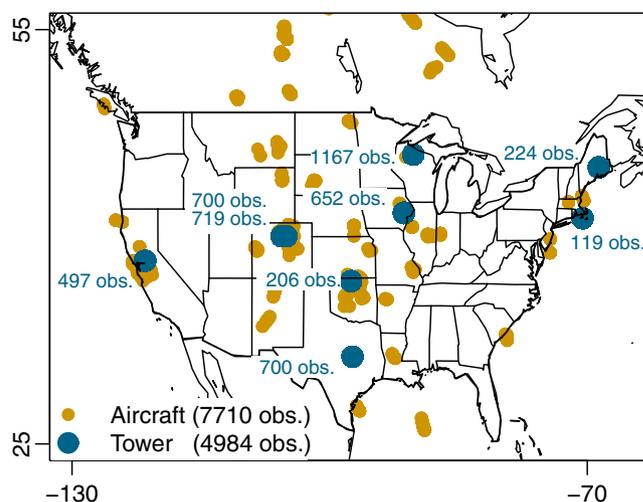

Fig. 2. CH_4 concentration measurements from 2007 and 2008 and the number of observations associated with each measurement type. Blue text lists the number of observations associated with each stationary tower measurement site.

a covariance function to describe the spatial and temporal correlation of the stochastic component and optimizes its spatial and temporal distribution simultaneously with the optimization of the activity datasets in the deterministic component (*SI Text*, Fig. S5) (26–28). Because of the stochastic component, the final emissions estimate can have a different spatial and temporal distribution from any combination of the activity data.

If the observation network is sensitive to a broad array of different source sectors and/or if the spatial activity maps are effective at explaining those sources, many activity datasets will be included in the deterministic model. If the deterministic model explains the observations well, the magnitude of CH_4 emissions in the stochastic component will be small, the assignment to specific sectors will be unambiguous, and uncertainties in the emissions estimates will be small. This result is not the case here, as discussed below (see *Results*).

A number of previous studies used top-down methods to constrain anthropogenic CH_4 sources from global (29–33) to regional (13–15, 34–38) scales over North America. Most regional studies adopted one of three approaches: use a simple box model to estimate an overall CH_4 budget (14), estimate a budget using the relative ratios of different gases (15, 37–39), or estimate scaling factors for inventories by region or source type (13, 34–36). The first two methods do not usually give explicit information about geographic distribution. The last approach provides information about the geographic distribution of sources, but results hinge on the spatial accuracy of the underlying regional or sectoral emissions inventories (40).

Here, we are able to provide more insight into the spatial distribution of emissions; like the scaling factor method above, we leverage spatial information about source sectors from an existing inventory, but in addition we estimate the distribution of emissions where the inventory is deficient. We further bolster attribution of regional emissions from the energy industry using the observed correlation of CH_4 and propane, a gas not produced by biogenic processes like livestock and landfills.

Results

Spatial Distribution of CH_4 Emissions. Fig. 3 displays the result of the 2-y mean of the monthly CH_4 inversions and differences from the EDGAR 4.2 inventory. We find emissions for the United States that are a factor of 1.7 larger than the EDGAR inventory. The optimized emissions estimated by this study bring the model closer in line with the observations (Fig. 4, Figs. S6 and S7). Posterior emissions fit the CH_4 observations [$R^2 = 0.64$, root mean square error (RMSE) = 31 ppb] much better than EDGAR

v4.2 ($R^2 = 0.23$, RMSE = 49 ppb). Evidently, the spatial distribution of EDGAR sources is inconsistent with emissions patterns implied by the CH_4 measurements and associated footprints.

Several diagnostic measures preclude the possibility of major systematic errors in WRF–STILT. First, excellent agreement between the model and measured vertical profiles from aircraft implies little bias in modeled vertical air mixing (e.g., boundary-layer heights) (Fig. 4). Second, the monthly posterior emissions estimated by the inversion lack statistically significant seasonality (Fig. S8). This result implies that seasonally varying weather patterns do not produce detectable biases in WRF–STILT. *SI Text* discusses possible model errors and biases in greater detail.

CH_4 observations are sparse over parts of the southern and central East Coast and in the Pacific Northwest. Emissions estimates for these regions therefore rely more strongly on the deterministic component of the flux model, with weights constrained primarily by observations elsewhere. Therefore, emissions in these areas, including from coal mining, are poorly constrained (*SI Text*).

Contribution of Different Source Sectors. Only two spatial activity datasets from EDGAR 4.2 are selected through the BIC as meaningful predictors of CH_4 observations over the United States: population densities of humans and of ruminants (Table S1). Some sectors are eliminated by the BIC because emissions are situated far from observation sites (e.g., coal mining in West Virginia or Pennsylvania), making available CH_4 data insensitive to these predictors. Other sectors may strongly affect observed concentrations but are not selected, indicating that the spatial datasets from EDGAR are poor predictors for the distribution of observed concentrations (e.g., oil and natural gas extraction and oil refining). Sources from these sectors appear in the stochastic component of the GIM (*SI Text*).

The results imply that existing inventories underestimate emissions from two key sectors: ruminants and fossil fuel extraction and/or processing, discussed in the remainder of this section.

We use the optimized ruminant activity dataset to estimate the magnitude of emissions with spatial patterns similar to animal husbandry and manure. Our corresponding US budget of 12.7 ± 5.0 TgC·y^{-1} is nearly twice that of EDGAR and EPA (6.7 and 7.0, respectively). The total posterior emissions estimate over the northern plains, a region with high ruminant density but little fossil fuel extraction, further supports the ruminant estimate (Nebraska, Iowa, Wisconsin, Minnesota, and South Dakota). Our total budget for this region of 3.4 ± 0.7 compares with 1.5 TgC·y^{-1} in EDGAR. Ruminants and agriculture may also be
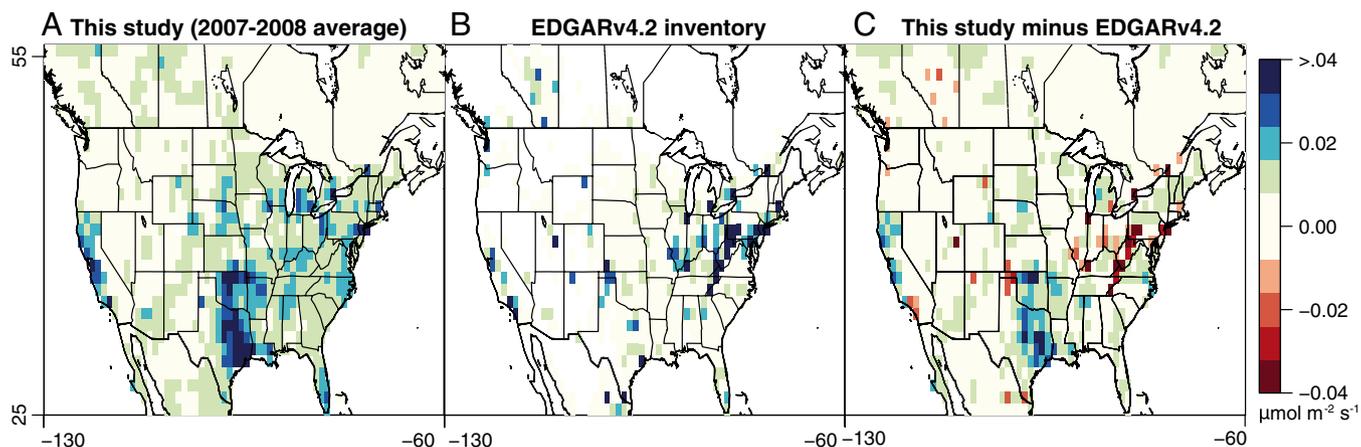
Fig. 3. The 2-y averaged CH_4 emissions estimated in this study (*A*) compared against the commonly used EDGAR 4.2 inventory (*B* and *C*). Emissions estimated in this study are greater than in EDGAR 4.2, especially near Texas and California.
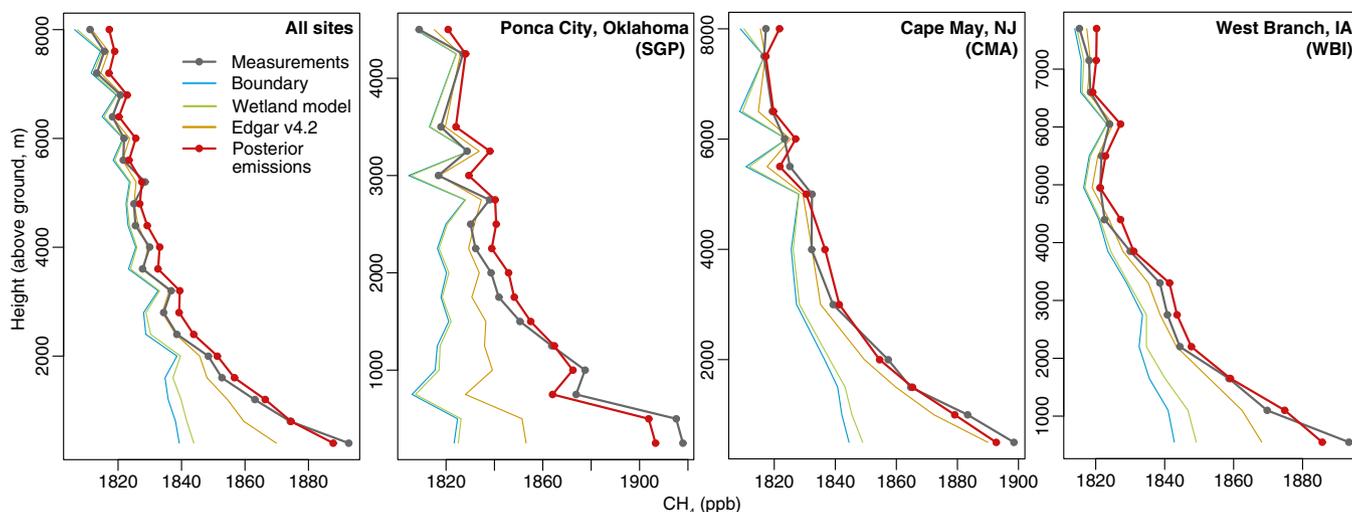
Fig. 4. A model–measurement comparison at several regular NOAA/DOE aircraft monitoring sites (averaged over 2007–2008). Plots include the measurements; the modeled boundary condition; the summed boundary condition and wetland contribution (from the Kaplan model); and the summed boundary, wetland, and anthropogenic contributions (from EDGAR v4.2 and the posterior emissions estimate).

partially responsible for high emissions over California (41). EDGAR activity datasets are poor over California (42), but several recent studies (34, 36–38, 41) have provided detailed top-down emissions estimates for the state using datasets from state agencies.

Existing inventories also greatly underestimate CH_4 sources from the south-central United States (Fig. 3). We find the total CH_4 source from Texas, Oklahoma, and Kansas to be 8.1 ± 0.96 $TgC \cdot y^{-1}$, a factor of 2.7 higher than the EDGAR inventory. These three states alone constitute ~24 ± 3% of the total US anthropogenic CH_4 budget or 3.7% of net US greenhouse gas emissions [in CO_2 equivalents (10)].

Texas and Oklahoma were among the top five natural gas producing states in the country in 2007 (18), and aircraft observations of alkanes indicate that the natural gas and/or oil industries play a significant role in regional CH_4 emissions. Concentrations of propane (C_3H_8), a tracer of fossil hydrocarbons (43), are strongly correlated with CH_4 at NOAA/DOE aircraft monitoring locations over Texas and Oklahoma ($R^2 = 0.72$) (Fig. 5). Correlations are much weaker at other locations in North America ($R^2 = 0.11$ to 0.64).

We can obtain an approximate CH_4 budget for fossil-fuel extraction in the region by subtracting the optimized contributions associated with ruminants and population from the total emissions. The residual ([Fig. S4C]) represents sources that have spatial patterns not correlated with either human or ruminant density in EDGAR. Our budget sums to 3.7 ± 2.0 $TgC \cdot y^{-1}$, a factor of 4.9 ± 2.6 larger than oil and gas emissions in EDGAR v4.2 (0.75 $TgC \cdot y^{-1}$) and a factor of 6.7 ± 3.6 greater than EDGAR sources from solid waste facilities (0.55 $TgC \cdot y^{-1}$), the two major sources that may not be accounted for in the deterministic component. The population component likely captures a portion of the solid waste sources so this residual methane budget more likely represents natural gas and oil emissions than landfills. *SI Text* discusses in detail the uncertainties in this sector-based emissions estimate. We currently do not have the detailed, accurate, and spatially resolved activity data (fossil fuel extraction and processing, ruminants, solid waste) that would provide more accurate sectorial attribution.

Katzenstein et al. (2003) (14) were the first to report large regional emissions of CH_4 from Texas, Oklahoma, and Kansas; they cover an earlier time period (1999–2002) than this study. They used a box model and 261 near-ground CH_4 measurements taken over 6 d to estimate a total Texas–Oklahoma–Kansas CH_4 budget (from all sectors) of 3.8 ± 0.75 $TgC \cdot y^{-1}$. We revise their
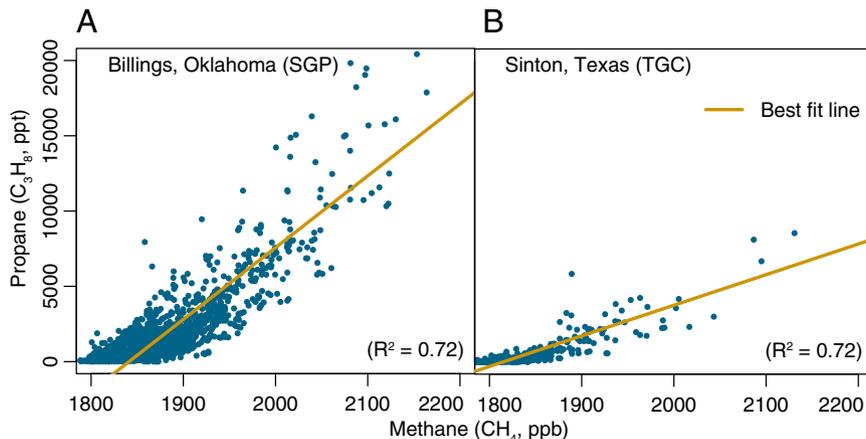

Fig. 5. Correlations between propane and CH_4 at NOAA/DOE aircraft observation sites in Oklahoma (*A*) and Texas (*B*) over 2007–2012. Correlations are higher in these locations than at any other North American sites, indicating large contributions of fossil fuel extraction and processing to CH_4 emitted in this region.

estimate upward by a factor of two based on the inverse model and many more measurements from different platforms over two full years of data. *SI Text* further compares the CH_4 estimate in Katzenstein et al. and in this study.

Discussion and Summary

This study combines comprehensive atmospheric data, diverse datasets from the EDGAR inventory, and an inverse modeling framework to derive spatially resolved CH_4 emissions and information on key source sectors. We estimate a mean annual US anthropogenic CH_4 budget for 2007 and 2008 of 33.4 ± 1.4 $TgC \cdot y^{-1}$ or ~7–8% of the total global CH_4 source. This estimate is a factor of 1.5 and 1.7 larger than EPA and EDGAR v4.2, respectively. CH_4 emissions from Texas, Oklahoma, and Kansas alone account for 24% of US methane emissions, or 3.7% of the total US greenhouse gas budget.

The results indicate that drilling, processing, and refining activities over the south-central United States have emissions as much as 4.9 ± 2.6 times larger than EDGAR, and livestock operations across the US have emissions approximately twice that of recent inventories. The US EPA recently decreased its CH_4 emission factors for fossil fuel extraction and processing by 25–30% (for 1990–2011) (10), but we find that CH_4 data from across North America instead indicate the need for a larger adjustment of the opposite sign.

EARTH, ATMOSPHERIC, AND PLANETARY SCIENCES

1. Butler J (2012) The NOAA annual greenhouse gas index (AGGI). Available at http://www.esrl.noaa.gov/gmd/aggi/. Accessed November 4, 2013.
2. Fiore AM, et al. (2002) Linking ozone pollution and climate change: The case for controlling methane. *Geophys Res Lett* 29:1919.
3. Jacob D (1999) *Introduction to Atmospheric Chemistry* (Princeton Univ Press, Princeton).
4. Mitchell LE, Brook EJ, Sowers T, McConnell JR, Taylor K (2011) Multidecadal variability of atmospheric methane, 1000-1800 CE. *J Geophys Res Biogeosci* 116:G02007.
5. Dlugokencky EJ, et al. (2009) Observational constraints on recent increases in the atmospheric CH_4 burden. *Geophys Res Lett* 36:L18803.
6. Sussmann R, Forster F, Rettinger M, Bousquet P (2012) Renewed methane increase for five years (2007-2011) observed by solar FTIR spectrometry. *Atmos Chem Phys* 12:4885–4891.
7. Kirschke S, et al. (2013) Three decades of global methane sources and sinks. *Nat Geosci* 6:813–823.
8. Wang JS, et al. (2004) A 3-D model analysis of the slowdown and interannual variability in the methane growth rate from 1988 to 1997. *Global Biogeochem Cycles* 18:GB3011.
9. Ciais P, et al. (2013) *Carbon and Other Biogeochemical Cycles: Final Draft Underlying Scientific Technical Assessment* (IPCC Secretariat, Geneva).
10. US Environmental Protection Agency (2013) *Inventory of U.S. Greenhouse Gas Emissions and Sinks: 1990–2011, Technical Report EPA 430-R-13-001* (Environmental Protection Agency, Washington).
11. Olivier JGJ, Peters J (2005) CO_2 from non-energy use of fuels: A global, regional and national perspective based on the IPCC Tier 1 approach. *Resour Conserv Recycling* 45:210–225.
12. European Commission Joint Research Centre, Netherlands Environmental Assessment Agency (2010) *Emission Database for Global Atmospheric Research (EDGAR)*, Release Version 4.2. Available at http://edgar.jrc.ec.europa.eu. Accessed November 4, 2013.
13. Kort EA, et al. (2008) Emissions of CH_4 and N_2O over the United States and Canada based on a receptor-oriented modeling framework and COBRA-NA atmospheric observations. *Geophys Res Lett* 35:L18808.
14. Katzenstein AS, Doezema LA, Simpson IJ, Blake DR, Rowland FS (2003) Extensive regional atmospheric hydrocarbon pollution in the southwestern United States. *Proc Natl Acad Sci USA* 100(21):11975–11979.
15. Pétron G, et al. (2012) Hydrocarbon emissions characterization in the Colorado Front Range: A pilot study. *J Geophys Res Atmos* 117:D04304.
16. Karion A, et al. (2013) Methane emissions estimate from airborne measurements over a western United States natural gas field. *Geophys Res Lett* 40:4393–4397.
17. Howarth RW, Santoro R, Ingraffea A (2011) Methane and the greenhouse-gas footprint of natural gas from shale formations. *Clim Change* 106:679–690.
18. US Energy Information Administration (2013) *Natural Gas Annual 2011,* Technical report (US Department of Energy, Washington).
19. National Research Council (2010) *Verifying Greenhouse Gas Emissions: Methods to Support International Climate Agreements* (National Academies Press, Washington).
20. Dlugokencky EJ, Nisbet EG, Fisher R, Lowry D (2011) Global atmospheric methane: Budget, changes and dangers. *Philos Trans A Math Phys Eng Sci* 369(1943):2058–2072.
21. Lin JC, et al. (2003) A near-field tool for simulating the upstream influence of atmospheric observations: The Stochastic Time-Inverted Lagrangian Transport (STILT) model. *J Geophys Res Atmos* 108(D16):4493.
22. Nehrkorn T, et al. (2010) Coupled Weather Research and Forecasting-Stochastic Time-Inverted Lagrangian Transport (WRF-STILT) model. *Meteorol Atmos Phys* 107:51–64.
23. NOAA ESRL (2013) *Carbon Cycle Greenhouse Gas Group Aircraft Program*. Available at http://www.esrl.noaa.gov/gmd/ccgg/aircraft/index.html. Accessed November 4, 2013.
24. Biraud SC, et al. (2013) A multi-year record of airborne CO_2 observations in the US southern great plains. *Atmos Meas Tech* 6:751–763.
25. Pan LL, et al. (2010) The Stratosphere-Troposphere Analyses of Regional Transport 2008 Experiment. *Bull Am Meteorol Soc* 91:327–342.
26. Kitanidis PK, Vomvoris EG (1983) A geostatistical approach to the inverse problem in groundwater modeling (steady state) and one-dimensional simulations. *Water Resour Res* 19:677–690.
27. Michalak A, Bruhwiler L, Tans P (2004) A geostatistical approach to surface flux estimation of atmospheric trace gases. *J Geophys Res Atmos* 109(D14):D14109.
28. Gourdji SM, et al. (2012) North American CO_2 exchange: Inter-comparison of modeled estimates with results from a fine-scale atmospheric inversion. *Biogeosciences* 9:457–475.
29. Chen YH, Prinn RG (2006) Estimation of atmospheric methane emissions between 1996 and 2001 using a three-dimensional global chemical transport model. *J Geophys Res Atmos* 111(D10):D10307.
30. Meirink JF, et al. (2008) Four-dimensional variational data assimilation for inverse modeling of atmospheric methane emissions: Analysis of SCIAMACHY observations. *J Geophys Res Atmos* 113(D17):D17301.
31. Bergamaschi P, et al. (2009) Inverse modeling of global and regional CH4 emissions using SCIAMACHY satellite retrievals. *J Geophys Res Atmos* 114(D22):D22301.
32. Bousquet P, et al. (2011) Source attribution of the changes in atmospheric methane for 2006-2008. *Atmos Chem Phys* 11:3689–3700.
33. Monteil G, et al. (2011) Interpreting methane variations in the past two decades using measurements of CH_4 mixing ratio and isotopic composition. *Atmos Chem Phys* 11:9141–9153.
34. Zhao C, et al. (2009) Atmospheric inverse estimates of methane emissions from central California. *J Geophys Res Atmos* 114(D16):D16302.
35. Kort EA, et al. (2010) Atmospheric constraints on 2004 emissions of methane and nitrous oxide in North America from atmospheric measurements and receptor-oriented modeling framework. *J Integr Environ Sci* 7:125–133.
36. Jeong S, et al. (2012) Seasonal variation of CH_4 emissions from central California. *J Geophys Res* 117:D11306.
37. Peischl J, et al. (2012) Airborne observations of methane emissions from rice cultivation in the Sacramento Valley of California. *J Geophys Res Atmos* 117(D24):D00V25.
38. Wennberg PO, et al. (2012) On the sources of methane to the Los Angeles atmosphere. *Environ Sci Technol* 46(17):9282–9289.
39. Miller JB, et al. (2012) Linking emissions of fossil fuel CO2 and other anthropogenic trace gases using atmospheric 14CO2. *J Geophys Res Atmos* 117(D8):D08302.
40. Law RM, Rayner PJ, Steele LP, Enting IG (2002) Using high temporal frequency data for CO_2 inversions. *Global Biogeochem Cycles* 16(4):1053.
41. Jeong S, et al. (2013) A multitower measurement network estimate of California's methane emissions. *J Geophys Res Atmos*, 10.1002/jgrd.50854.
42. Xiang B, et al. (2013) Nitrous oxide (N2O) emissions from California based on 2010 CalNex airborne measurements. *J Geophys Res Atmos* 118(7):2809–2820.
43. Koppmann R (2008) *Volatile Organic Compounds in the Atmosphere* (Wiley, Singapore).

Miller et al.

Supporting Information

Miller et al. 10.1073/pnas.1314392110

SI Text

This supplement contains further explanation of the modeling and statistical methods and provides additional model validation.

Atmospheric Modeling Approach

Transport Model Overview. This study uses STILT, the Stochastic Time-Inverted Lagrangian Transport model, for all atmospheric transport simulations (1). Model runs use an ensemble of 500 particles followed 10 d back in time. The methane increments computed from continental surface sources are added to the methane boundary condition, the concentration of methane in air masses before being influenced by emissions in North America.

The model equation can be written as (2)

$$z = \mathbf{H}s + \varepsilon, \qquad [\text{S1}]$$

where z (dimensions $n \times 1$) is the contribution of continental sources to the observation sites, and s ($m \times 1$) are the true, unknown methane emissions. Any estimate of the unknown emissions (s) is termed $\hat{s}$. The total methane concentration measured at the tower or aircraft is given by $z + b$, where b ($n \times 1$) is the boundary condition. The influence footprint $\mathbf{H}$ gives the concentration enhancement at the measurement site due to unit emission flux from each grid cell. The footprint has units of concentration per surface flux, or parts per billion (ppb) per $\mu \text{mol} \cdot \text{m}^{-2} \cdot \text{s}^{-1}$. Each row of $\mathbf{H}$ ($n \times m$) is the footprint associated with an individual methane measurement. Finally, ε ($n \times 1$) describes model–data mismatch errors, all model or measurement errors that are unrelated to an imperfect emissions estimate. In other words, this mismatch remains the same irrespective of the emissions estimate ($\hat{s}$) used in the model. The mismatch includes, but is not limited to, errors in modeled transport, the methane boundary condition (b), and the methane measurements. Common inversion frameworks based on Gaussian statistics, including this one, assume that all model–data mismatch errors (ε) are random with a mean of zero and a covariance described by the $n \times n$ matrix $\mathbf{R}$.

STILT trajectories are driven by the Weather Research and Forecasting model (WRF, version 2.1.2) meteorological fields (3, 4). Our WRF simulations consist of sequential 30-h meteorological forecasts initiated daily from NARR (North American Regional Reanalysis). All simulations include convection using a Grell–Devenyi scheme (5). These wind fields use a nested resolution: 10 km over most of the continental United States and 40 km over other North American regions.

Methane Boundary Condition. The boundary condition (b) could be constructed either from interpolated measurements or from the output of a global chemical tracer model (such as Geos-Chem). We choose the former approach due to uncertainties associated with the global distribution of methane emissions.

We construct the boundary condition using a two-stage process. First, we use an empirical methane boundary curtain over the Pacific Ocean as an initial guess for b. This western curtain consists of National Oceanic and Atmospheric Administration (NOAA) measurements near or over the Pacific Ocean, interpolated latitudinally, vertically, and daily using a curve-fitting procedure (6). The individual trajectories in every 500-trajectory STILT simulation typically end at different locations and reach the western boundary at different latitudes, times, or elevations. The mean statistics of the trajectory ensemble at the western

curtain provide the initial value for b. Most of the STILT back-trajectories in this study reach the Pacific coastline less than 10 d after leaving the observation site (64%). One hundred percent of trajectories originating from the Walnut Grove, California (WGC) site, 83% of those originating at Erie, Colorado (BAO), 60% at West Branch, Iowa (WBI), and 60% from Moody, Texas (WKT) reach the Pacific Ocean. The Martha's Vineyard and Argyle, Maine, sites have the lowest fraction of trajectories that reach the Pacific Ocean (37% and 32%, respectively) although many of the remaining trajectories never exit the continent during the 10-d span of the trajectory run.

Second, we use NOAA aircraft observations over North America in the free troposphere (>3,000 m) to fit the initial boundary estimate to regional conditions or airflow patterns. The adjustment is most relevant for observation sites farther from the western curtain (e.g., Massachusetts and Maine). We calculate, for different regions and seasons, the mean model-observation difference above 3,000 m using the initial boundary guess and Emissions Database for Global Atmospheric Research (EDGAR) v4.2. Regions include the western, eastern, south-central, and north-central portions of the United States over winter, spring, summer, and fall. The purpose of this adjustment is twofold. First, it accounts for the inflow of "clean background" air that may enter a region outside the prevailing westerlies. Second, it accounts for the small amount of methane oxidation that may occur en route between the western boundary curtain and the methane measurement sites. This aircraft-based adjustment has a mean of −2.7 ppb and a maximum magnitude of −7 ppb. An inversion using the initial western boundary curtain without the regional adjustment estimates methane budgets of 32.0 and 7.7 TgC·y^{-1} for the United States and Texas–Oklahoma–Kansas, respectively, within about 5% of the final best estimate in the main article.

The boundary condition exhibits marked seasonality, with an average 40 ppb peak in winter. This peak reflects large-scale seasonal changes in Northern Hemisphere clean-air concentrations.

WRF–STILT does not explicitly model atmospheric oxidation processes. We fit the boundary condition to local or regional free troposphere values, eliminating the need to consider longer range oxidation chemistry. Furthermore, the footprint ($\mathbf{H}$) is greatest within 2–3 d of the associated measurement. Methane has a global-averaged lifetime of 7–11 y (7, 8), implying methane decay of less than 1–1.5 ppb over these 2- to 3-d time scales.

Study Time Period. We choose 2007–2008 as the time frame of this study for two reasons. First, there are no daily methane measurements from US tower sites before mid-2006, with the exception of the Niwot, Colorado sites. Weekly to monthly methane observations are available at some sites before 2006. Second, the WRF meteorology fields used here are available only through 2008. These fields are validated by Nehrkorn et al. (2010) (4) and used in a number of existing studies (9–12), but they have a limited time scope.

Observations. We use diverse methane measurements taken at tall towers or by aircraft during 2007–2008. Measurements include daily flask samples from the NOAA/DOE tower network (weekly at Argyle and Ponca City): Argyle, Maine [AMT, 45°N, 69°W, 107 m above ground level (agl)]; Erie, Colorado (BAO, 40°N, 105°W, 300 m agl); Park Falls, Wisconsin (LEF, 46°N, 90°W, 244 m agl), Martha's Vineyard, Massachusetts (MVY, 41°N, 71°W, 12 m agl); Niwot Ridge and Niwot Forest, Colorado (NWF,

NWR, 40°N, 105°W, 2, 3, 23 m agl); Ponca City, Oklahoma (SGP, 37°N, 97°W, 60 m agl); West Branch, Iowa (WBI, 42°N, 93°W, 379 m agl); Walnut Grove, California (WGC, 38°N, 121°W, 91 m agl), and Moody, Texas (WKT, 31°N, 97°W, 122, 457 m agl) (Fig. 2). The inverse model incorporates surface data and aircraft measurements up to 2,500 m agl; observations at higher altitudes are less sensitive to surface emissions and are reserved for model validation and adjustment of the boundary condition. The flask and aircraft data are sampled only during the daytime hours so this study is not affected by the large uncertainties associated with modeling the nocturnal boundary layer (13, 14).

Statistical Methods

We use a geostatistical inverse modeling (GIM) framework to estimate monthly methane emissions (s) for 2007 and 2008 on a 1° × 1° latitude–longitude grid (15–17):

$$s = \mathbf{X}\boldsymbol{\beta} + \mathcal{N}(\mathbf{0}, \mathbf{Q}). \qquad \text{[S2]}$$

The GIM uses a deterministic model ($\mathbf{X}\boldsymbol{\beta}$) for the prior estimate of emissions, similar to a multiple regression. Each column of $\mathbf{X}$ is a different spatial dataset, including a column for a constant component, and $\boldsymbol{\beta}$ is the vector of associated unknown coefficients. This setup differs from a Bayesian synthesis inversion, which typically uses a prior with a static, known magnitude (18, 19).

The GIM also has a stochastic component, described by a multivariate normal distribution $\mathcal{N}$ with a mean of zero and covariance matrix $\mathbf{Q}$. This component describes all emissions that do not fit the spatial pattern of the deterministic model. Unlike most Bayesian synthesis inversions, the GIM accounts for spatial and/or temporal correlation (i.e., covariance) in the stochastic component by including off-diagonal terms in $\mathbf{Q}$.

The GIM framework allows the atmospheric observations to determine the spatial patterns of both the deterministic and stochastic components. Also, the formulation ensures that the prior has no overall bias, an important statistical assumption of most inversion frameworks. A number of existing studies have used this approach successfully for trace gas surface flux estimation (11, 12, 17, 20, 21).

The best estimate of emissions (s) is typically the minimum of the geostatistical cost function (17):

$$L_{s,\beta} = \frac{1}{2}\ln|\mathbf{Q}| + \frac{1}{2}\ln|\mathbf{R}| + \frac{1}{2}(z - \mathbf{H}s)^T \mathbf{R}^{-1}(z - \mathbf{H}s)$$
$$+ \frac{1}{2}(s - \mathbf{X}\boldsymbol{\beta})^T \mathbf{Q}^{-1}(s - \mathbf{X}\boldsymbol{\beta}). \qquad \text{[S3]}$$

This cost function, based on Gaussian statistics, cannot preclude large negative emissions, and we use Lagrange multipliers to enforce nonnegativity (22, 23). Large negative emissions would be unrealistic for methane given that the soil sink is only ~4% of global methane loss (24). Any soil sink over the United States would be far smaller than the posterior uncertainties and therefore not detectable by the inversion framework with any degree of certainty. Lagrange multipliers, the method used to enforce nonnegativity, is iterative and produces a robust estimate of the posterior emissions subject to physical bounds. However, the resulting posterior uncertainties are generally too large and should be interpreted with caution. A recent paper discusses this method in detail and the impact on the final emissions estimate (23).

Covariance Matrix Estimation. Restricted maximum likelihood (REML) provides an objective way to estimate the structure and magnitude of the error covariance matrices in the inversion ($\mathbf{R}$

and $\mathbf{Q}$); it guarantees that the actual inversion residuals match against those predicted in the covariance matrices (17, 25).

REML estimates the parameters ($\boldsymbol{\theta}$) that define $\mathbf{R}$ and $\mathbf{Q}$ by minimizing a modified form of the cost function in Eq. S3. In practice, it may be difficult to estimate the covariance matrix parameters ($\boldsymbol{\theta}$) using Eq. S3 directly because this function also depends on the unknown values of the fluxes (s) and the drift coefficients ($\boldsymbol{\beta}$). The restricted likelihood integrates over all possible values of s and $\boldsymbol{\beta}$. The integration effectively removes s and $\boldsymbol{\beta}$ from the cost function, and the function is subsequently reformulated only in terms of the covariance matrices and several known pieces of information (see ref. 25 for a full derivation):

$$L_{\boldsymbol{\theta}} = -\ln \int_{\boldsymbol{\beta}} \int_s p(s, \boldsymbol{\beta}, \boldsymbol{\theta}|z, \mathbf{H}) \, ds \, d\boldsymbol{\beta}$$
$$\qquad \text{[S4]}$$
$$= \frac{1}{2}\ln|\boldsymbol{\Psi}| + \frac{1}{2}\ln|\mathbf{X}^T\mathbf{H}^T\boldsymbol{\Psi}^{-1}\mathbf{H}\mathbf{X}| + \frac{1}{2}z^T\boldsymbol{\Xi}z$$

$$\boldsymbol{\Psi} = \mathbf{H}\mathbf{Q}\mathbf{H}^T + \mathbf{R} \qquad \text{[S5]}$$

$$\boldsymbol{\Xi} = \boldsymbol{\Psi}^{-1} - \boldsymbol{\Psi}^{-1}\mathbf{H}\mathbf{X}(\mathbf{X}^T\mathbf{H}^T\boldsymbol{\Psi}^{-1}\mathbf{H}\mathbf{X})^{-1}\mathbf{X}^T\mathbf{H}^T\boldsymbol{\Psi}^{-1}. \qquad \text{[S6]}$$

where $p(s, \boldsymbol{\beta}, \boldsymbol{\theta}|z, \mathbf{H})$ is the joint probability of the fluxes, coefficients, and covariance matrix parameters. The optimal covariance matrix parameters are those that minimize the above equation, typically estimated with an iterative Gauss–Newton algorithm. Many studies from geostatistics and other fields indicate that REML is one of the most accurate and unbiased methods for estimating errors and/or the structural parameters of a statistical model (26–33). Among other advantages, it ensures that the weighted sum of squares residuals from the inversion will follow the expected χ^2 distribution (26).

In this study, we construct the covariance matrix $\mathbf{R}$ as a diagonal matrix. To estimate the diagonal elements of $\mathbf{R}$ ($\sigma_{\mathbf{R}}^2$, the model–data mismatch variance), we first calculate the variance of the model–measurement residuals for each measurement site when the STILT model is run with the EDGAR v. 3.2 FT2000 anthropogenic emissions inventory. Two top-down studies find that this inventory has the correct overall magnitude over the United States (9, 34), and thus we use this version of EDGAR over others as a starting point in error estimation. We then use REML to estimate a single scaling factor to align the initial estimate with the variances suggested by the atmospheric data.

The estimation of $\mathbf{Q}$ follows a slightly different form. The setup here estimates a constant value for the a priori variance (the diagonal elements). In other words, we assume there is little spatial or temporal variability in the variance in the stochastic component of the emissions estimate, an assumption that makes sense given large emissions in disparate regions of the United States and apparent absence of large seasonality in anthropogenic sources. Other parameters of $\mathbf{Q}$ to estimate include l, the decorrelation length parameter, and t, the decorrelation time parameter (where $3l$ and $3t$ are the total approximate decorrelation length and time, respectively). REML would not converge on a decorrelation length for the off-diagonal elements of $\mathbf{Q}$. This result may be due to geographic heterogeneity in the correlation lengths of the stochastic component. We set a decorrelation length parameter (l) at 100 km, a compromise between emissions uncertainties that might be correlated over the distance of a large urban area and uncertainties in agricultural emissions that may be correlated over a larger regional scale. Test inversions with $l = 50$, 300, and 500 km provide a measure of the sensitivity of the estimated fluxes to the choice of the decorrelation parameter. Ultimately, the choice of l

has little impact on the total US anthropogenic budget (less than 1 TgC·y^{-1}).

Using REML, we estimate a variance in the stochastic component of 0.041 ± 0.001 μmol ·m^{-2}·s^{-1} (i.e., the square root of the diagonal elements of $\mathbf{Q}$). The decorrelation time and length parameters in the exponential covariance function are estimated at $t = 36 \pm 5$ d and $l = 100$ km, respectively.

The Deterministic Model. The GIM setup here adopts spatial activity datasets from the EDGAR inventory as predictors ($\mathbf{X}$) for the distribution of methane emissions (see the list of spatial activity data in *Model and Observation Framework* in the main article) and uses atmospheric data to estimate the associated emission factors ($\boldsymbol{\beta}$). The emissions factors in existing inventories can be highly uncertain and have recently changed by up to 50% in EDGAR for sectors such as coal and natural gas (35) (Fig. S1).

We use a model selection method to assemble an optimal set of spatial activity datasets for the inversion. These methods will select as many predictors for use in $\mathbf{X}$ that can explain variability in the data but will prevent an over-fit or unreliable coefficient estimates (36, 37). We implement one of the most common methods, the Bayesian information criterion (BIC) (11, 38, 39). The BIC numerically scores all possible combinations of activity datasets based on how well they improve goodness of fit (i.e., the log-likelihood of the model, similar to the weighted sum of squares) and applies an increasing penalty for model complexity. For each additional activity dataset, the penalty increases with the natural log of number of observations. The best candidate model ($\mathbf{X}$) is the one with the lowest BIC score (11):

$$\hat{\beta} = \left(\mathbf{X}^T\mathbf{H}^T\boldsymbol{\Psi}^{-1}\mathbf{H}\mathbf{X}\right)^{-1}\mathbf{X}^T\mathbf{H}^T\boldsymbol{\Psi}^{-1}z \qquad \textbf{[S7]}$$

$$BIC = \ln|\boldsymbol{\Psi}| + \left(z - \mathbf{H}\mathbf{X}\hat{\beta}\right)^T\boldsymbol{\Psi}^{-1}\left(z - \mathbf{H}\mathbf{X}\hat{\beta}\right) + p\ln(n), \qquad \textbf{[S8]}$$

where p is the number of predictors (number of columns in $\mathbf{X}$), and n is the number of methane measurements.

The drift coefficients ($\boldsymbol{\beta}$) in the model of the mean must be positive because a spatial dataset should never contribute negatively to the posterior methane emissions. Therefore, we eliminate all candidate models from consideration that yield negative coefficients.

The BIC does not support hypothesis testing with P values, but the difference in BIC scores provides a metric of confidence (40). A score difference greater than 2 indicates notable evidence against the higher scoring model, and a score increment greater than 10 indicates "very strong" evidence against that model.

Only two spatial datasets from EDGAR are identified by the BIC as important predictors of methane observations over the United States:

$$\beta_0 + \beta_1[\text{population density}] + \beta_2[\text{ruminant density}]$$

Where β_0, β_1, and β_2 are the coefficients of the spatial activity data. The first term, β_0, represents the mean of all sources with spatial patterns other than population or ruminant density. Table S1 provides example BIC scores for this and other candidate models, including what are commonly considered the largest methane source sectors. The BIC scores strongly suggest that there is either insufficient data to include more than two activity datasets or that several existing activity datasets do not adequately describe the methane observations. In particular, the table indicates that the observation network is not sufficiently sensitive to coal sources and that the oil and gas production activity datasets from EDGAR do not accurately represent the

spatial distribution of the methane emissions consistent with observations.

Fig. S4 displays the methane budget from each of the spatial datasets in the deterministic model (e.g., scaled by the estimated coefficients, $\hat{\beta}$). It is important to note that population density serves as a proxy for a number of source sectors that are colocated with population (e.g., natural gas distribution, landfills, and wastewater treatment) at the 1° spatial scale. Additionally, fuel extraction and animal husbandry are colocated over Texas and Oklahoma so some emissions assigned to ruminant density (Fig. S4A) may instead partially reflect fossil fuel industry sources.

Uncertainty Analysis

General Uncertainties in the Model and Measurements. Fig. S2 provides a visualization of the model–data mismatch errors estimated by REML (σ_R, the SD of ε). This mismatch includes random model and measurement errors unrelated to the emissions: errors in the wind fields, boundary layer height, methane boundary condition, and spatial/temporal aggregation, among other error sources. Model–data mismatch typically ranges from 40% to 70% of the total methane emissions signal seen at each tower, but the relative mismatch is higher at "clean air" sites like Niwot Ridge, Colorado (NWF/NWR). Absolute uncertainties are largest at measurement sites close to mountain ranges (e.g., BAO and WGC). Those uncertainties likely reflect difficulties in modeling wind fields near complex topography. Over Texas and Oklahoma, where the estimated anthropogenic methane emissions are among the largest in the United States, the model–data mismatch is just under half the magnitude of the total average methane signal.

Uncertainties in the Emissions Estimate. The posterior covariance matrices (denoted V) provide a measure of uncertainty in the estimated emissions ($\hat{s}$) and estimated coefficients ($\hat{\beta}$) (17):

$$\begin{bmatrix} \mathbf{V}_{\hat{s}} & \mathbf{V}_{\hat{s}\beta} \\ \mathbf{V}_{\hat{\beta}\hat{s}} & \mathbf{V}_{\hat{\beta}} \end{bmatrix} = \begin{bmatrix} \mathbf{Q}^{-1} + \mathbf{H}^T\mathbf{R}^{-1}\mathbf{H} & \mathbf{Q}^{-1}\mathbf{X} \\ \mathbf{X}^T\mathbf{Q}^{-1} & \mathbf{X}^T\mathbf{Q}^{-1}\mathbf{X} \end{bmatrix}^{-1}. \qquad \textbf{[S9]}$$

Eq. S9 is the inverse of the Hessian of the cost function (Eq. S3). The posterior covariance matrices, summed across different months and locations, produce the confidence intervals on the methane budgets listed throughout the paper. All uncertainties listed are $2\sigma_{\hat{s}}$ and $2\sigma_{\hat{\beta}}$, unless otherwise noted.

The uncertainties in the emissions estimate vary depending on the temporal or spatial scales of interest. For example, the uncertainties can be larger than the estimated emissions at the 1° latitude–longitude spatial scale and monthly temporal scale. However, uncertainties decrease as the emissions estimate is averaged over larger regions and longer times (Fig. S5). Intuitively, the uncertainties are higher at finer spatial/temporal scales because the atmospheric methane data have limited capacity to determine the precise location or time of grid-scale emissions. The methane data, however, can indicate regional or national average emissions with greater confidence. Mathematically, the uncertainties per unit area decrease at aggregated spatial/temporal scales because the covariances in the posterior covariance matrix are often negative. Therefore, at aggregated scales, the mean of the variances/covariances is usually smaller.

The covariance matrix $\mathbf{V}_{\hat{s}}$ encompasses most but not all uncertainties in the emissions estimate. It accounts for uncertainties in the drift coefficients ($\hat{\beta}$) and in the stochastic component of the emissions, and it accounts for uncertainty due to randomly distributed model–data mismatch errors ($\varepsilon = \mathcal{N}(\mathbf{0}, \mathbf{R})$) (Eq. S1). However, existing statistical inversions cannot explicitly account for model–data mismatch errors that produce overall bias (i.e., if ε has a nonzero mean). Potential

bias-type errors in WRF–STILT are discussed separately throughout the remainder of *SI Text*.

Wetland Sources. We model the wetland contribution using the Kaplan wetland inventory (41, 42), scaled in magnitude to match the observations as in refs. 42 and 43. This signal (about 9 ppb in late summer, 2.0 Tg C TgC·y^{-1} for the continental United States) is then removed from z to subtract the influence of wetland sources from the data. Wetlands make only small contributions to the signals at most of the observation sites in the United States and thus cannot be reliably constrained in the inversion. After this subtraction, the inversion produces optimized anthropogenic budgets with little seasonal variation (Fig. S8). Because wetland emissions are strongly seasonal, this result indicates that our procedure does not produce wetland-related biases.

We also run a separate test inversion using the Dynamic Land Ecosystem Model (DLEM) for wetland subtraction instead of the Kaplan model (43–45) (also 2.0 TgC·y^{-1} for the continental United States). This test inversion produces a US anthropogenic methane budget of 34.1 TgC·y^{-1} and a south-central US budget of 8.1 TgC·y^{-1}, very similar to the results using Kaplan wetland emissions. Therefore, we conclude that our results are independent of the source model used to account for wetland emissions.

Furthermore, wetland models predict only small to modest emissions over the largest source regions in our study. Two recent studies compare wetland methane fluxes for a number of biogeochemical models (46, 47). None of the models put significant wetland emissions over Texas or Oklahoma, both relatively dry regions, where our study found large methane emissions. Existing land maps indicate wetlands along the Mississippi River and Delta, but modeled wetland emissions in this region are nonetheless five times smaller than the anthropogenic sources estimated by our study in this area (46, 47). The correlation between methane concentrations and propane in the south-central region additionally reinforces the attribution of high CH$_4$ fossil-fuel extraction and processing.

Geological Sources. Several studies report methane emissions from geological degassing, including ground seepage, geothermal emissions, and volcanic emissions (48–50). This study does not account for geological sources explicitly, but previous studies indicate that these fluxes would be small compared with the magnitude of US anthropogenic emissions. The estimated magnitude of this source ranges from 2.2–9% of total global emissions (48–50). One study estimates that terrestrial geological sources, in particular, contribute 1.1–2.8% of the global methane budget, and most emissions are attributable to volcanic activity and mud volcanoes (48). A few mud volcanos exist along the California coastline, but these geological features are otherwise uncommon over the continental United States (51). Based upon this information, we estimate at most an ~5% uncertainty in the emissions derived here due to geological degassing.

Uncertainties in Sector-Based Emissions Estimates. This section analyzes in greater depth the uncertainties in sector-based emissions estimates (e.g., for ruminants or the approximate fossil-fuel budget). These uncertainties, listed in the main article, are calculated using the covariance matrices for $\hat{\beta}$ and $\hat{s}$ (Eq. S9), summed to large spatial and annual temporal scales. The uncertainties on the sector-based budget estimates are large due to uncertainties in $\hat{\beta}$. The coefficients describe emissions with spatial patterns similar to the activity data, and colocated source sectors or errors in the activity datasets make the coefficient estimates ($\hat{\beta}$) less definitive. For example, ruminants and fossil fuel extraction have similar distributions over the south-central United States so some of the emissions assigned to ruminants in the deterministic model could instead be from the Texas and Oklahoma fossil-fuel extraction sector. Similarly, if landfill emissions do not always coincide with population, then some landfill emissions may appear in the ruminant (Fig. S4A), mean, or stochastic components (Fig. S4C) instead of the population component (Fig. 2B). Therefore, the atmospheric methane data provides strong constraints on total emissions at the regional or national scale, but estimates by source sector often have larger confidence intervals.

We run a test inversion to investigate the possible effects of spatial correlation between ruminants and other source sectors. In this test inversion, we estimate different emissions factors ($\hat{\beta}$) for ruminants over four different regions of the United States: the western (CA, OR, WA, NV, ID, MT, AZ, UT, WY, NM, CO), the midwest (NE, SD, ND, MN, IA, MO, WI, IL, MI, IN), the south-central (TX, OK, KS, LA, AK), and the eastern United States (MS, TN, KY, AL, FL, GA, NC, SC, VA, WV, OH, PA, NY, MD, NJ, CT, VT, NY, NH, MA, RI, ME). Any differences in emissions factors by region represent one of three possibilities. First, emissions factors for agriculture may differ due to regional agricultural practices or climate. Second, the range may be caused by differences in the spatial distribution of the ruminant activity dataset from actual agricultural emissions. Third, the range may represent uncertainties caused by source sectors colocated with ruminants. Our agriculture emissions factors in the test case are lowest over the west and midwest (1.25 and 1.3 times EDGAR, respectively) and highest over the south-central United States (2.6 times EDGAR). We repeat the calculation of south-central US nonagriculture and nonpopulation emissions. In the main article, we estimate this budget at 3.7 ± 2.0 TgC·y^{-1}, a budget that could represent oil and gas emissions or unaccounted landfills. If we apply the western US ruminant emissions factor to Texas, Oklahoma, and Kansas, we obtain a higher estimate for this fossil fuel and/or landfill budget of 4.74 TgC/y. Alternately, if we apply the south-central US ruminant emissions factor to Texas, Oklahoma, and Kansas, we obtain a lower estimate for the fossil fuel and/or landfill budget of 2.94 TgC/y. These estimates are within the confidence intervals listed in the main article for ruminants and fossil-fuel extraction and/or ruminants. Note that the different setup for **X** in this test case does not affect total posterior methane budgets in each region by more than 1%; changes in the configuration of **X** only affects emissions attribution by sector.

Model Capability and Validation

This section further validates the WRF–STILT model, the estimated methane budget, and discusses the geographic coverage of the methane observations.

Model Transport and Footprint Validation. The WRF fields in this study are validated extensively by Nehrkorn et al. (4), and several pertinent statistics are included here. The WRF simulations are set up specifically to conserve mass and do so by a factor of ten better than other meteorological products like the National Centers for Environmental Prediction (NCEP) global analysis fields [Final (FNL)] (4). Compared with US and Canadian radiosondes, horizontal winds in WRF exhibit a root mean squared error (RMSE) of 2.5–4 m/s with no change in error statistics at the top of the planetary boundary layer (4).

Several previous inversion studies with STILT estimate emissions that are consistent across different meteorologies and compared with Eulerian models. This fact further validates model transport and indicates a lack of overall bias in the WRF–STILT footprints (**H**). Miller et al. (12) use both WRF and the Regional Atmospheric Modeling System (RAMS) with STILT to estimate US nitrous oxide emissions; the US budgets match within $12 \pm 6\%$ (12). Furthermore, STILT studies of carbon monoxide and methane produce budgets comparable with top-down emissions estimates with the Geos–Chem model. Constraints on summertime

US carbon monoxide emissions with RAMS–STILT and Geoschem match to within 10% (52, 53), and methane budgets for the Hudson Bay Lowland in Canada estimated with WRF–STILT and Geos–Chem are similar within 5% (42, 43).

Validation of the Methane Boundary Condition. Methane measurements from aircraft show good agreement with modeled concentrations, notably above 3,000 m where regional surface emissions have little influence (Fig. 4 in the main article). At these altitudes, the mean measurement–posterior model difference is 2.8 ppb, with a SD of 18 ppb. These statistics reflect uncertainties in the modeled boundary condition but also reflect uncertainties in the modeled vertical gradient and in advection or convection of heterogeneous air masses in the upper free troposphere.

To test the effect of a 2.8-ppb uncertainty, we subtract this amount from the boundary condition and reestimate the emissions. This test inversion produces US and south-central budgets of 35.4 ± 1.4 and 8.4 ± 1.0 TgC·y^{-1}, respectively. Given these uncertainties, the methane budgets presented in this study may be slightly low by 3–9%.

Comparison Against Aircraft and Tower Data. Regular methane observations from the NOAA aircraft monitoring network help validate the vertical model structure (i.e., planetary boundary layer height and convection). The comparison in Fig. 4 of the main article indicates several notable features of the model. First, the close match between model and observations in the free troposphere above 3,000 m confirms the suitability of the two-stage methane boundary condition, as discussed earlier. Second, the vertical structure in the model matches well against observations (to within 20 ppb at any aircraft sampling location).

Two additional figures provide further model–data comparison. First, Fig. S6 compares modeled methane concentrations against time series of measurements at the NOAA tower locations. As discussed in the main article, the EDGAR inventory underestimates emissions in California (WGC tower) and Texas (WKT tower) more severely than in other geographic regions of the United States. Second, Fig. S7 compares all methane observations used in the inversion (from aircraft and tall tower locations) against modeled concentrations. Both Figs. S6 and S7 highlight the improved data–model fit given by the posterior emissions estimate.

The Utility of Aircraft Data in the Inversion. To gauge the utility of aircraft data in the inversion, we run a test GIM using only observations from the ground sites. This inversion estimates a US methane budget of 37.4 ± 3.0 TgC·y^{-1} and Texas–Oklahoma–Kansas budget of 9.6 ± 1.3 TgC·y^{-1}. This test inversion produces emission fields that bleed into sparsely populated areas adjacent to large source regions (e.g., surrounding Texas and California).

However, modeled concentrations using this test emissions estimate are too high within the free troposphere compared with aircraft data. As a result, we infer that an estimated US budget from an inversion without aircraft data would likely be too high by 7–17%. The aircraft data bound the vertical redistribution of surface emissions. Without this bound, the inversion may inaccurately estimate emissions that agree with surface methane measurement but nevertheless result in too much methane in the free troposphere and emission fields that spread too far across the landscape.

Geographic Coverage. Fig. S3 visualizes the average footprint (**H**) of the methane measurement network in 2007 and 2008. The figure confirms that the observation network is sensitive to emissions over much of the central and western United States but insensitive to coal or urban-related emissions in the mid and southern Atlantic states. In particular, the sparsity of observations near West Virginia and Pennsylvania inhibits a strong constraint on East Coast coal emissions. US EPA estimates that coal constitutes 11% of all methane emissions, and approximately one third of all US coal production is in Appalachia (54, 55). Consequently, we estimate that a paucity of observations over Appalachia may contribute a 1–3% uncertainty in the total US methane budget.

Comparison with the Methane Estimate from Katzenstein et al. (56). A steady increase in the number of US gas wells between 2001 and 2007–2008 may partially explain the differences between this study and Katzenstein et al. (56). The total number of wells in Texas, for example, increased by ~58% over this time period (57).

Several aspects of our inverse-modeling study also allow a more extensive picture of emissions than available to previous studies. The NOAA/DOE observations from a diverse set of measurement platforms characterize the atmospheric distribution of methane over a multiyear period. We note that concentrations measured weekly at the NOAA Texas (WKT) tower from 2001 to 2003 average ~80 ppb higher than ground-level observations near the WKT site during the Katzenstein et al. study (56). A stationary front on the Texas–Oklahoma border and strong convection over Texas during the 5-d measurement period may have lofted methane plumes higher into the troposphere, beyond detection at the surface. The WRF–STILT model simulates the temporal and spatial variation in advection, convection, and boundary-layer dynamics, consistent with meteorological data. This detailed characterization of the atmosphere accounts for methane plumes that are not uniformly mixed within the lower troposphere. Therefore, the comprehensive NOAA/DOE methane measurements and our GIM provide perspective on national emissions and source sectors not possible in previous efforts.

1. Lin JC, et al. (2003) A near-field tool for simulating the upstream influence of atmospheric observations: The Stochastic Time-Inverted Lagrangian Transport (STILT) model. *J Geophys Res Atmos* 108(D16):4493.
2. Gerbig C, et al. (2003) Toward constraining regional-scale fluxes of CO_2 with atmospheric observations over a continent: 2. Analysis of COBRA data using a receptor-oriented framework. *J Geophys Res Atmos* 108(D24):4757.
3. Skamarock W, et al. (2005) *A Description of the Advanced Research WRF Version 2* (National Center for Atmospheric Research, Boulder, CO), Technical Report NCAR/TN–468+STR.
4. Nehrkorn T, et al. (2010) Coupled Weather Research and Forecasting-Stochastic Time-Inverted Lagrangian Transport (WRF-STILT) model. *Meteorol Atmos Phys* 107:51–64.
5. Grell GA, Devenyi D (2002) A generalized approach to parameterizing convection combining ensemble and data assimilation techniques. *Geophys Res Lett* 29:381–384.
6. Thoning K, et al. (1989) Atmospheric carbon dioxide at Mauna Loa observatory 2. Analysis of the NOAA GMCC data, 1974–1985. *J Geophys Res* 94:8549–8565.
7. Prather MJ, Holmes CD, Hsu J (2012) Reactive greenhouse gas scenarios: Systematic exploration of uncertainties and the role of atmospheric chemistry. *Geophys Res Lett* 39(9):L09803.
8. Ciais P, et al. (2013) *Carbon and Other Biogeochemical Cycles: Final Draft Underlying Scientific Technical Assessment* (IPCC Secretariat, Geneva).

9. Kort EA, et al. (2010) Atmospheric constraints on 2004 emissions of methane and nitrous oxide in North America from atmospheric measurements and receptor-oriented modeling framework. *J Integr Environ Sci* 7:125–133.
10. Huntzinger DN, Gourdji SM, Mueller KL, Michalak AM (2011) The utility of continuous atmospheric measurements for identifying biospheric CO_2 flux variability. *J Geophys Res* 116(D6):D06110.
11. Gourdji SM, et al. (2012) North American CO_2 exchange: Inter-comparison of modeled estimates with results from a fine-scale atmospheric inversion. *Biogeosciences* 9:457–475.
12. Miller SM, et al. (2012) Regional sources of nitrous oxide over the United States: Seasonal variation and spatial distribution. *J Geophys Res Atmos* 117(D6):D06310.
13. Matross DM, et al. (2006) Estimating regional carbon exchange in New England and Quebec by combining atmospheric, ground-based and satellite data. *Tellus B Chem Phys Meteor* 58:344–358.
14. Gourdji SM, et al. (2010) Regional-scale geostatistical inverse modeling of North American CO_2 fluxes: A synthetic data study. *Atmos Chem Phys* 10:6151–6167.
15. Kitanidis PK, Vomvoris EG (1983) A geostatistical approach to the inverse problem in groundwater modeling (steady state) and one-dimensional simulations. *Water Resour Res* 19:677–690.

16. Snodgrass M, Kitanidis P (1997) A geostatistical approach to contaminant source identification. *Water Resour Res* 33:537–546.
17. Michalak A, Bruhwiler L, Tans P (2004) A geostatistical approach to surface flux estimation of atmospheric trace gases. *J Geophys Res Atmos* 109(D14):D14109.
18. Rodgers C (2000) *Inverse Methods for Atmospheric Sounding: Theory and Practice, Series on Atmospheric, Ocean, and Planetary Physics* (World Scientific, Singapore).
19. Tarantola A (2005) *Inverse Problem Theory and Methods for Model Parameter Estimation* (Society for Industrial and Applied Mathematics, Philadelphia).
20. Mueller KL, Gourdji SM, Michalak AM (2008) Global monthly averaged CO_2 fluxes recovered using a geostatistical inverse modeling approach: 1. Results using atmospheric measurements. *J Geophys Res Atmos* 113(D21):D21114.
21. Gourdji SM, Mueller KL, Schaefer K, Michalak AM (2008) Global monthly averaged CO_2 fluxes recovered using a geostatistical inverse modeling approach: 2. Results including auxiliary environmental data. *J Geophys Res Atmos* 113(D21):D21115.
22. Gill PE, Murray W H. WM (1981) *Practical Optimization* (Academic, London).
23. Miller SM, Michalak AM, Levi PJ (2013) Atmospheric inverse modeling with known physical bounds: An example from trace gas emissions. *Geosci Model Dev Discuss* 6: 4531–4562.
24. Dutaur L, Verchot LV (2007) A global inventory of the soil CH_4 sink. *Global Biogeochem Cycles* 21(4):GB4013.
25. Kitanidis PK (1986) Parameter uncertainty in estimation of spatial functions: Bayesian analysis. *Water Resour Res* 22:499–507.
26. Kitanidis PK (1983) Statistical estimation of polynomial generalized covariance functions and hydrologic applications. *Water Resour Res* 19(4):909–921.
27. Robinson DL (1987) Estimation and use of variance components. *J R Stat Soc Series D* 36:3–14.
28. Kitanidis PK (1987) Parametric estimation of covariances of regionalized variables. *J Am Water Resour Assoc* 23:557–567.
29. McGilchrist C (1989) Bias of ML and REML estimators in regression models with ARMA errors. *J Statist Comput Simulation* 32:127–136.
30. Wilson GT (1989) On the use of marginal likelihood in time series model estimation. *J R Stat Soc Series B Stat Methodol* 51:15–27.
31. Cheang WK, Reinsel GC (2000) Bias reduction of autoregressive estimates in time series regression model through restricted maximum likelihood. *J Am Stat Assoc* 95: 1173–1184.
32. Lark RM, Cullis BR (2004) Model-based analysis using REML for inference from systematically sampled data on soil. *Eur J Soil Sci* 55:799–813.
33. Lark RM, Cullis BR, Welham SJ (2006) On spatial prediction of soil properties in the presence of a spatial trend: the empirical best linear unbiased predictor (e-blup) with REML. *Eur J Soil Sci* 57:787–799.
34. Kort EA, et al. (2008) Emissions of CH_4 and N_2O over the United States and Canada based on a receptor-oriented modeling framework and COBRA-NA atmospheric observations. *Geophys Res Lett* 35:L18808.
35. European Commission Joint Research Centre, Netherlands Environmental Assessment Agency (2010) *Emission Database for Global Atmospheric Research (EDGAR)*, Release Version 4.2. Available at http://edgar.jrc.ec.europa.eu. Accessed November 4, 2013.
36. Zucchini W (2000) An introduction to model selection. *J Math Psychol* 44(1):41–61.
37. Konishi S, Kitagawa G (2008) *Information Criteria and Statistical Modeling,* Springer Series in Statistics (Springer, New York).
38. Schwarz G (1978) Estimating the dimension of a model. *Ann Stat* 6:461–464.
39. Mueller KL, Yadav V, Curtis PS, Vogel C, Michalak AM (2010) Attributing the variability of eddy-covariance CO_2 flux measurements across temporal scales using geostatistical regression for a mixed northern hardwood forest. *Global Biogeochem Cycles* 24(3):GB3023.
40. Kass R, Raftery A (1995) Bayes factors. *J Am Stat Assoc* 90:773–795.
41. Kaplan J (2002) Wetlands at the Last Glacial Maximum: Distribution and methane emissions. *Geophys Res Lett*, 10.1029/2001GL013366.
42. Pickett-Heaps CA, et al. (2011) Magnitude and seasonality of wetland methane emissions from the Hudson Bay Lowlands (Canada). *Atmos Chem Phys* 11:3773–3779.
43. Miller S, et al. (2013) Observational constraints on the distribution, seasonality, and environmental predictors of North American boreal methane emissions. *Global Biogeochem Cycles*, in press.
44. Tian H, et al. (2010) Spatial and temporal patterns of CH_4 and N_2O fluxes in terrestrial ecosystems of North America during 1979-2008: Application of a global biogeochemistry model. *Biogeosciences* 7:2673–2694.
45. Tian H, et al. (2011) Net exchanges of CO_2, CH_4, and N_2O between China's terrestrial ecosystems and the atmosphere and their contributions to global climate warming. *J Geophys Res Biogeosci* 116(G2):G02011.
46. Melton JR, et al. (2013) Present state of global wetland extent and wetland methane modelling: conclusions from a model inter-comparison project (WETCHIMP). *Biogeosciences* 10:753–788.
47. Wania R, et al. (2013) Present state of global wetland extent and wetland methane modelling: Methodology of a model inter-comparison project (WETCHIMP). *Geosci Model Dev* 6:617–641.
48. Judd AG, Hovland M, Dimitrov LI, García Gil S, Jukes V (2002) The geological methane budget at continental margins and its influence on climate change. *Geofluids* 2: 109–126.
49. Kvenvolden KA, Rogers BW (2005) Gaia's breath—global methane exhalations. *Mar Petroleum Geol* 22:579–590.
50. Etiope G, Lassey KR, Klusman RW, Boschi E (2008) Reappraisal of the fossil methane budget and related emission from geologic sources. *Geophys Res Lett* 35(9):L09307.
51. Dimitrov LI (2002) Mud volcanoes: The most important pathway for degassing deeply buried sediments. *Earth Sci Rev* 59:49–76.
52. Hudman RC, et al. (2008) Biogenic versus anthropogenic sources of CO in the United States. *Geophys Res Lett* 35(4):L04801.
53. Miller SM, et al. (2008) Sources of carbon monoxide and formaldehyde in North America determined from high-resolution atmospheric data. *Atmos Chem Phys* 8: 7673–7696.
54. US Environmental Protection Agency (2013) *Inventory of U.S. Greenhouse Gas Emissions and Sinks: 1990–2011* (Environmental Protection Agency, Washington), Technical Report EPA 430-R-13-001.
55. Young P (2012) *Annual Coal Report 2011* (Office of Oil, Gas, and Coal Supply Statistics, US Energy Information Administration, Washington, DC), Technical Report.
56. Katzenstein AS, Doezema LA, Simpson IJ, Blake DR, Rowland FS (2003) Extensive regional atmospheric hydrocarbon pollution in the southwestern United States. *Proc Natl Acad Sci USA* 100(21):11975–11979.
57. US Energy Information Administration (2013) *Natural Gas Annual 2011* (US Energy Information Administration, Washington), Technical Report.
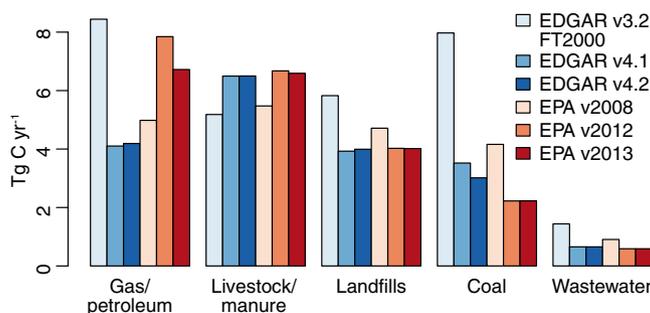
Fig. S1. US methane emissions by sector from several existing inventories. All methane budgets are from the year 2005 except EDGAR v3.2 FT2000, which estimates emissions from 2000.
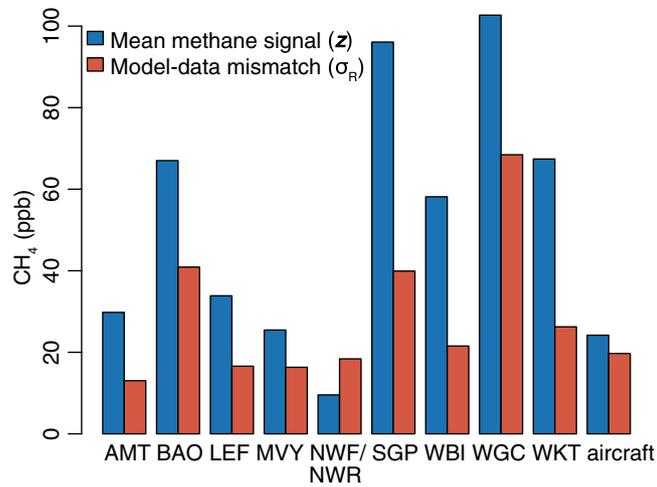
Fig. S2. A visualization of the estimated model–data mismatch across different methane measurement sites, compared against the 2-y averaged contribution from anthropogenic emissions at each site (z, the concentration measurements minus the boundary condition and modeled wetland contribution).
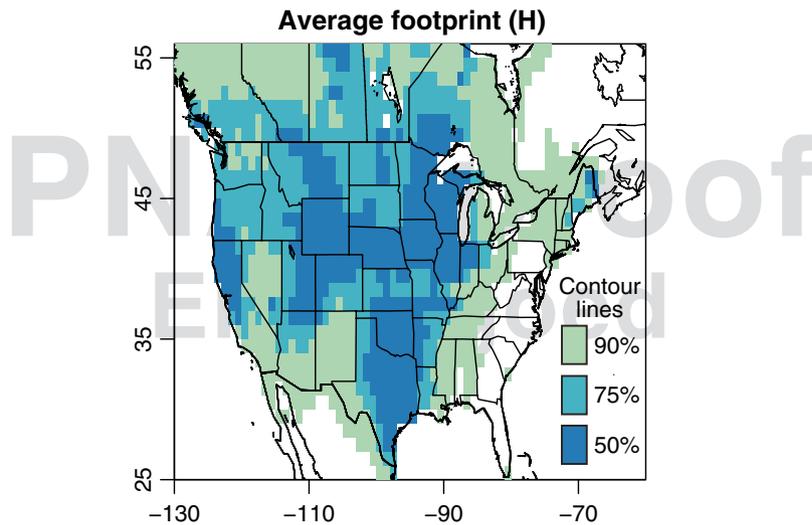

Fig. S3. The footprint of the 2007–2008 methane observation network (i.e., **H**, averaged by row). Contour lines represent the percentage of the summed observation network footprint that is encapsulated by the given area. In other words, this figure illustrates the extent to which emissions in different locations are "seen" by the observation network and provides a sense of the network's ability to constrain sources across different regions.
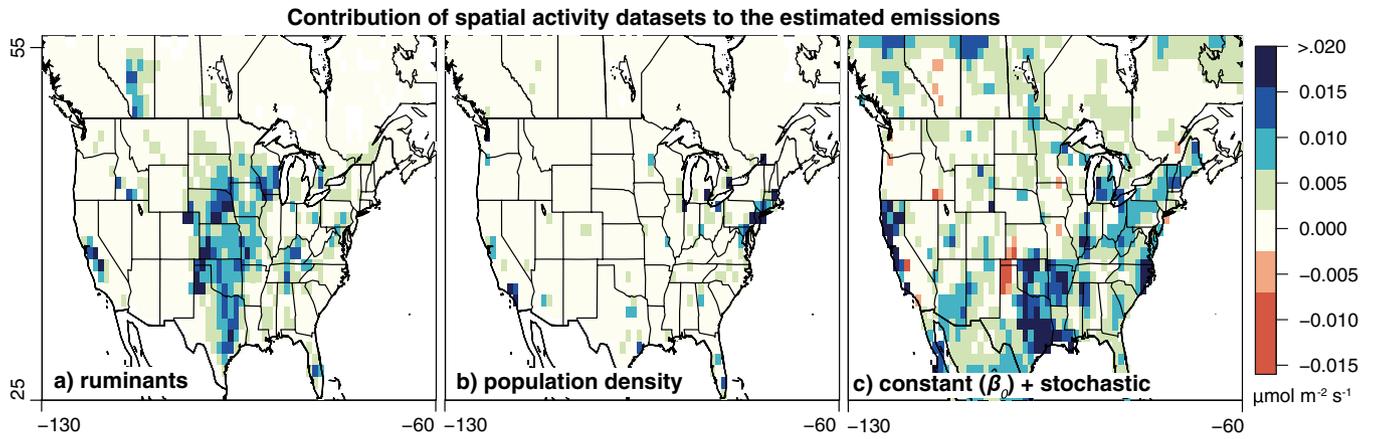
Contribution of spatial activity datasets to the estimated emissions

a) ruminants
b) population density
c) constant (β_0) + stochastic

μmol m^{-2} s^{-1}

Fig. S4. The contribution of different activity datasets to the overall emissions estimate. The sum of the constant and stochastic components (*C*) includes all sources not described by the spatial activity datasets (the sum of *A* and *B*). The contribution of the activity datasets (*A* and *B*) is constant throughout the 2 y, and the stochastic component (*C*) changes by month (averaged in the plot here).

(a) Aggregated in time

(b) Aggregated in space

Mean
Range

Uncertainty (μmol m^{-2} s^{-1})
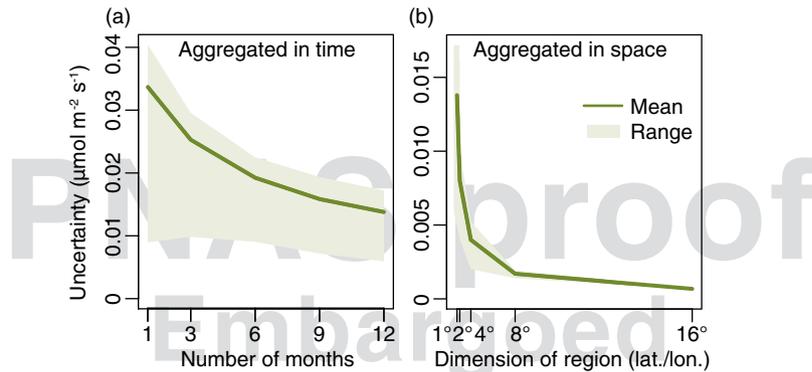
Number of months

Dimension of region (lat./lon.)

Fig. S5. The methane emissions estimate in this study has a 1° latitude–longitude spatial resolution and monthly temporal resolution. The uncertainty in the emissions estimate declines as the estimate is averaged to greater spatial and temporal scales. *A* shows how uncertainties over the south-central United States decrease as the grid-scale estimate is aggregated in time. *B* displays how the uncertainties decrease as the annual-average estimate is averaged spatially. Uncertainties listed are σ_s.
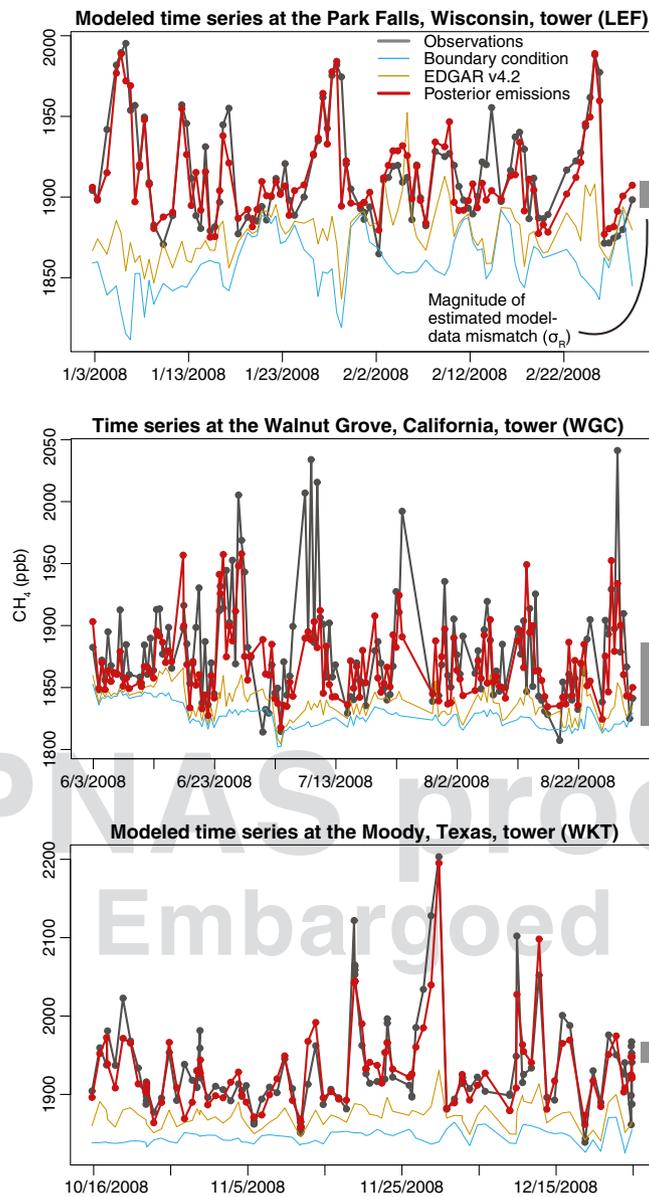
Fig. S6. A model–measurement comparison at several tower sites. The EDGAR v4.2 and posterior model plots include the boundary condition, wetland contribution modeled from the Kaplan inventory, and the anthropogenic contribution modeled from EDGAR and the posterior emissions, respectively.
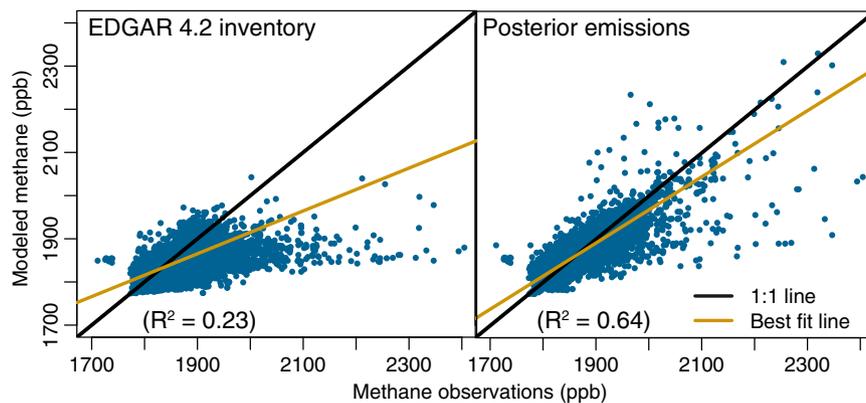

Fig. S7. A model–data comparison scatter plot for the posterior emissions estimate and EDGAR 4.2.
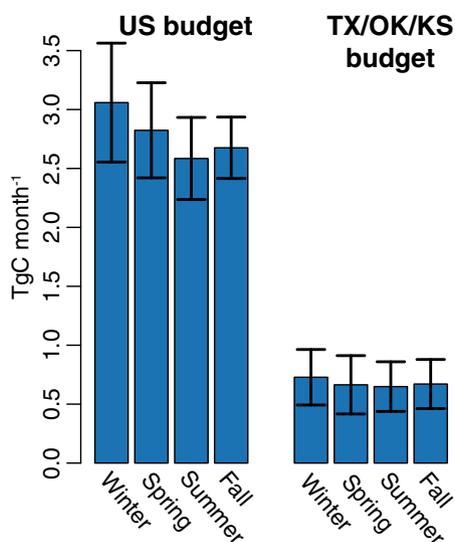
Fig. S8. Monthly anthropogenic methane budgets by season and associated uncertainties. The lack of strong seasonality implies minimal modeling errors due to wetland emissions, seasonal boundary condition biases, or seasonal wind field biases.

Table S1.   BIC scores for sample of candidate models

Candidate model	Score
Population + ruminants	96,825
Population + ruminants + oil/gas production	96,924
Population + ruminants + coal	96,925
Pop. + ruminants + oil/gas prod. + coal + rice	96,942

We test all combinations of the spatial activity data from EDGAR 4.2 (refer to *Model and Observation Framework* in the main article). We show only selected examples here that include what are commonly considered the largest methane source sectors.